Journal of

Materials Chemistry A

ARTICLE

Iodide-reduced Graphene Oxide with Dopant-free Spiro-OMeTAD for Ambient Stable and High-efficiency Perovskite Solar Cells

Qiang Luo,[‡a] Ye Zhang,[‡a] Chengyang Liu,[a] Jianbao Li,[a, b] Ning Wang[*c] and Hong Lin[*a]

Hygroscopic Li-bis(trifluoromethane)sulfonyimide (Li-TFSI) and corrosive pyridine doped 2, 2', 7, 7'-tetrakis(N, N-di-p-methoxy-phenylamine)-9, 9'-spirobifluorene (spiro-OMeTAD) in perovskite solar cells generally results in poor device ambient stability due to moisture-induced degradation of the perovskite absorber. Simultaneous fulfilling good ambient stability and high efficiency, this work proposes the use of a p-type, highly conductive reduced graphene oxide (RGO) reduced by ferrous iodide acid solution, combined with dopant-free spiro-OMeTAD as hole extraction and transport material in perovskite solar cells, achieving a maximum power conversion efficiencies (PCE) of 10.6%, greatly outperforming the reference devices based on pure dopant-free spiro-OMeTAD (PCE=6.5%). Impressively, only a 15% PCE degradation is observed for the device with RGO/dopant-free spiro-OMeTAD without encapsulation after 500 h, whereas the PCE drops by 65% for the device with Li-TFSI and pyridine doped spiro-OMeTAD. This work represents a significant step toward the realization of stable and high-efficiency perovskite solar cells.

Introduction

Solution-processed organic-inorganic hybrid trihalide perovskite solar cells have attracted significant research interests owing to their potential for low-cost fabrication of large-area devices and compatibility with light-weight and flexible plastic substrates.[1] In present, highly efficient perovskite solar cells typically employ an organic-inorganic metal halide perovskite material as both light absorber and charge transporter, which is sandwiched between an electron-blocking p-type organic hole transport layer and an n-type electron-transport layer.[2-4] With meticulous compositional engineering of perovskite materials, device interface design and film growth technique, perovskite solar cells have delivered impressive power conversion efficiencies (PCE) of over 17%.[5-7] In most state-of-the-art high-performance perovskite solar cells, a p-type organic small molecular, 2, 2', 7, 7'-tetrakis(N, N-di-p- methoxyphenyl-amine)-9, 9'-spirobifluorene (spiro-OMeTAD) was typically used as hole transport material (HTM).

The sp^3 hybridization of the nitrogen atom in spiro-OMeTAD leads to inherent triangular pyramid configuration hence large intermolecular distances, which results in low hole mobility and poor conductivity.[8,9] The low intrinsic charge carrier mobility and poor conductivity of spiro-OMeTAD is detrimental to photovoltaic performance of perovskite solar cells because they can cause additional series resistance and significant charge recombination. It

has therefore been a prevalent practice to incorporate a redox-active p-type dopant Li-bis(trifluoromethane)sulfonyimide (Li-TFSI) to invoke an oxidative process to reach appreciable conductivity for spiro-OMeTAD.[10-12] In addition, pyridine derivative was also used as additive to suppress charge recombination and to improve the contact between perovskite and HTM in perovskite solar cells.[13] However, such doping would necessitate an open system to allow for rather non-quantifiable oxygen ingression and unpredictable variations of oxidized spiro-OMeTAD concentration.[14] The hygroscopic properties of Li-TFSI salt would induce degradation of the perovskite layer if devices are not fully sealed against moisture[15,16] and the pyridine derivative is also corrosive to perovskite materials,[13] which could thus explain the wide variance in term of photovoltaic performance, reproducibility, and device stability.

Therefore, seeking novel HTMs without Li-TFSI and pyridine dopants such as 4-$tert$-butylpyridine,[15,17-20] or stable additives combined with HTMs such as spiro-OMeTAD or poly(3-hexylthiophene) (P3HT) for efficient and stable perovskite solar cells,[16,21-23] is highly desirable for the commercialization of perovskite solar cells. For example, a novel iridium complex, IrCp*Cl(PyPyz)[TFSI] has been used as additive for spiro-OMeTAD in perovskite solar cells, leading to improved cell performance and remarkable device stability in comparison to the unmodified and Co complex ((Co(PyPyz)$_3$[TFSI]$_3$) modified devices.[22] Recently,

graphdiyne as conductive additive to P3HT HTM for perovskite solar cells has been reported, the unsealed device stored in a desiccator retained 90% of its initial PCE.[21] Bamboo-structure carbon nanotubes was added to Li-TFSI and pyridine doped P3HT as HTM in perovskite solar cells yielded a maximum PCE of 8.3%, whereas the cell stability was not investigated.[24] In addition, sequentially deposited bilayers of P3HT functionalized single-walled carbon nanotubes (SWNTs) and dopant-free spiro-OMeTAD or PMMA also were used as HTM to replace doped spiro-OMeTAD for perovskite solar cells with the stabilized maximum power outputs of 10.7% were obtained. [15,16] During 500 h stability test the PCE retained 80% of its initial values when encapsulated with epoxy resin and a glass coverslip in a nitrogen-filled glove box.[16] However, different from graphdiyne or carbon nanotubes functioning only as conductive additives to facilitate hole transport in the composite film, P3HT functionalized SWNTs could be used as efficient HTM for perovskite solar cells due to not only their highly conductive but also their selective hole extraction properties. These results suggest the potential use of conductive additives or hole-extraction p-type carbon materials for fully replacing Li-TFSI and pyridine doping of spiro-OMeTAD and yielding comparably efficient but more stable devices.

Graphene, similar to its carbon nanotube counterpart, has unique properties such as high conductivity, ease of modification and low cost, and has already shown great potential in perovskite solar cells application.[25] As an oxygen-containing derivative of graphene, graphene oxide (GO) has recently been demonstrated to act as effective alternative for PEDOT:PSS in inverted heterojunction perovskite solar cells which has achieved a PCE of over 10%.[26] In spite of the great advantages of low manufacturing cost and compatibility with roll-to-roll processing, the photovoltaic performance of perovskite solar cells with GO as HTM is highly sensitive to the film thickness of GO due to its insulating and hygroscopic property.[26] Alternatively, an ultra-thin reduced graphene oxide (RGO) functionalized with p-hydrazinobenzenesulfonic acid was just recently reported as an efficient hole extracting material for inverted heterojunction perovskite solar cells,[27] with an improved device performance (maximum PCE of 10.8%) due to higher conductivity (~ 300 S m^{-1}) and optimal energy level alignment compared to GO and with a moderate stability (~ 60% of the initial value after 140 h in air).

Herein, we demonstrate p-type solution-processable RGO combined with dopant-free spiro-OMeTAD could be used as an efficient HTM in perovskite solar cells with superior stability and high-efficiency. The HTM was fabricated by spin-coating RGO dispersion on the perovskite film and consequently dopant-free spiro-OMeTAD was casted. By using such a bilayer structure, the maximum power conversion efficiency of perovskite solar cells reached up to 10.6%, much higher than the efficiency of cells containing GO/dopant-free spiro-OMeTAD, 6.1%, and dopant-free spiro-OMeTAD alone, 6.5%. In addition, devices with RGO showed a superior stability (over 85% remain of the initial value after 500 h in air). These results demonstrate the possibility to achieve almost identical device performance at massively reduced cost, using reduced graphene oxide prepared from solution-based method rather than prohibitive P3HT functionalized carbon nanotubes, and produce ambient stable perovskite solar cells. Furthermore, the charge extraction ability of RGO with or without dopant-free spiro-OMeTAD when interfaced with perovskite has been investigated and the hole transport pathways in perovskite solar cells are also discussed.

Experimental

Reduction of GO to RGO

GO was prepared using a modified Hummers' and Offeman's method from natural graphite. The GO dispersed in deionized water was reduced by using FeI$_2$ aqueous solution as reported in our previous work.[28] FeI$_2$ aqueous solution was synthesized directly from the reaction of iodine/iron powder with some drops of water as a catalyzer. Briefly, 5 g sphere-shaped iodine particles were grinded into fine powder in an agate mortar and subsequently mixed fully with 5 g fine iron powder in a beaker. Then 20 mL of deionized water were quickly added into the above beaker. By collecting the supernatant, the FeI$_2$ aqueous solution was obtained. After that, the resultant supernatant was added to a beak containing 100 mL 0.1 g mL^{-1} GO dispersion. Then, the pH value of the GO dispersion in FeI$_2$ aqueous solution was tuned by adding concentrated hydrochloric acid. To obtain different reduction degree of RGO, pH was tuned to 1, 1.5, 2 and 3 by controlling the volume of concentrated hydrochloric acid. Finally, the different GO acid dispersions were heated to 95 °C for 6 h to obtain various RGO. After the beakers containing RGO was cooled down to room temperature naturally, the resulting RGO dispersion was collected through centrifugation and washed with deionized water, and then sonicated in ethanol and washed with ethanol to remove the surface-absorbing residues. Finally, the wet product was dried by vacuum freeze-drying for 24 h and the resultant powder was further dried at 100 ºC in a vacuum drying cabinet for 48 h. For simplicity, the GO were reduced at pH=1, 1.5, 2, and 3 was designated as RGO-1, RGO-1.5, RGO-2, and RGO-3, respectively. To obtain dry GO power, the water in GO aqueous dispersion was removed by vacuum freeze-drying and then dried at 100 ºC in a vacuum drying cabinet for 48 h.

Device fabrication

Fluorine-doped tin oxide (FTO) conducting glass was etched with zinc power and diluted hydrochloric acid to form two detached electrode and subsequently being ultrasonically cleaned with detergent, deionized water, acetone and isopropanol, separately. Before the fabrication of solar cells, the cleaned FTO glass was treated with an ultraviolet/O$_3$ cleaner for at least 15 min. A compact TiO$_2$ layer was obtained by spin-coating an acidic solution of titanium isopropoxide in anhydrous ethanol on cleaned FTO surface, and then sintering at 500 °C for 30 min. A mesoporous layer was deposited on compacting layer by spin-coating a commercial colloidal dispersion of TiO$_2$ paste (20 nm, PST-18NR, JGC Catalysts and Chemicals Ltd., Japan, diluted with ethanol at a weight of 1/3.5) at 5000 rpm for 45s, and then drying at 125°C for 10 min, and further annealing in air at 500 °C for 30 min. After the mesoporous film was cooled down to room temperature, PbI$_2$ dissolved in N, N-dimethylformamide (1.2 M) was deposited on the mesoporous film by spin-coating at 5000 rpm for 60s, followed by drying at 100 °C on a hot plate for 45 min. After that, the resultant PbI$_2$ films were dipped into a solution of CH$_3$NH$_3$I in 2-propanol (12 mg mL^{-1}) for 10 min and then rinsed with 2-propanol and dried at 70 °C for 1 h.

For the preparation of RGO or GO dispersion, 50 mg of the as-obtained RGO or GO powder was dispersed in 50 mL chlorobenzene and sonicated in a bath sonicator for 2 h. The dispersion was subsequently centrifuged for 25 min at 10000 rpm to remove large RGO or GO particles. The precipitate was discarded while the supernatant was recovered. The obtained supernatant was further sonicated for 1 h to fully disperse the RGO or GO sheets. After the sonication, RGO aggregates were then removed by centrifugation at 12000 rpm for 15 min and the supernatant was recovered. The resultant RGO or GO dispersion with a concentration of about 0.05-0.08 mg mL^{-1} was used as stock solution for spin-coating.

For the fabrication of RGO or GO-based HTM layer, the RGO was firstly deposited dynamically on the as-prepared perovskite surface

by slow drop-to-drop spin-coating 600 μL RGO or GO dispersion at 2000 rpm for 120 s. Followed immediately by the deposition of 60 μL spiro-OMeTAD/chlorobenzene (30 mg mL^{-1}) by spin-coating at 4000 rpm for 60 s. Samples were then left in dry air for 12 h. After that, top electrode was deposited by thermal evaporation of Au. In stability study, the perovskite solar cells were stored in dark without any encapsulation. The average humidity percentage was about 40±7% and the temperature was about 20±3 $^{\circ}$C.

For doped spiro-OMeTAD deposition, 60 μl of 1 mL chlorobenzene solution containing 73.2 g spiro-OMeTAD, 18.5μl 4-*tert*-butylpyridine and 29 μL lithium bis(trifluoromethylsyfonyl)imide/acetonitrile (520 mg mL^{-1}) was cast onto the perovskite coated substrate and spun at a rate of 4000 rpm for 60 s.

Characterizations

The photocurrent–voltage (*J-V*) characteristics of the perovskite solar cells were measured with a digital source meter (2400, Keithley Instruments, USA) under AM 1.5G illumination (100 mW cm^{-2}), which was realized by a solar simulator (91192, Oriel, USA, calibrated with a standard crystalline silicon solar cell). The solar cells were masked with a metal aperture defining the active area (0.06 cm^2) of the solar cells. *J–V* curves were measured by scanning from forward bias to short circuit (FB-SC, from 1.3V to -0.1V) or from short circuit to forward bias (SC-FB, from -0.1V to 1.3V) with a scan rate of 0.022 V s^{-1}. The incident photon to current efficiency (IPCE) was characterized by using the QEX10 solar cell quantum efficiency measurement system (QEX10, PV measurements, USA). Prior to measurement, a standard silicon solar cell was used as reference.

The top surface morphology of the film was obtained using an LEO 1530 Gemini field emission scanning electron microscope (FESEM). The X-ray photoelectron spectroscopy (XPS) spectra were performed on X-ray photoelectron spectrometer (ESCALAB 250Xi, Thermo Fisher SCIENTIFIC INC., USA) with Al Kα radiation (*hv* = 1486.6 eV) as source. The compressed-powder RGO sheets were obtained by pressing the RGO power samples into a cylindrical tablet at a pressure of 8 MPa, whose conductivity (1 × 1 cm in size) was measured by a digital four-point probe system (SX1934, Suzhou, China) at room temperature. To get reliable conductivity data, four different sites of each sample were measured by the four-point probe system. The thickness of compressed-powder RGO sheets were measured by Tesa probe (Tesa GT21, Swiss) and the average thickness was utilized to calculate the conductivity. The Hall measurement (HL5500PC, NANOMETRICS, USA) was performed at room temperature to obtain the semiconductor type and carrier mobility of the compressed-powder RGO sheets using the Vander Pauw method. The mobility and semiconductor type for GO are not determined due to the limited sensitivity of the Hall measurement apparatus.

Steady-state photoluminescence (PL) spectra were acquired with a FLS920 transient optical spectrometer (Edinburgh Instruments, UK). The probe light is provided by a pulsed Xenon arc lamp. The sample was kept at a 45° angle to the excitation beam. The excitation and luminescence measurement was taken from the glass side for all tested samples. The sample for PL measurement was prepared as follows: perovskite film was deposited on cleaned glass, followed by drying at 100 °C on a hot plate. After that, the different quenchers were then deposited via spin-coating. Finally, to avoid the degradation of perovskite during the measurements, a layer of poly(methylmethacrylate) (PMMA) dissolved in chlorobenzene were then deposited via spin-coating.

Results and discussion

The as-reduced RGO exhibited a wrinkled paper-like structure, which was mainly composed of multilayered sheets (Fig. S1†). For simplicity, the GO were reduced at pH=1, 1.5, 2, and 3 was designated as RGO-1, RGO-1.5, RGO-2, and RGO-3. Fig. 1a shows the XPS spectra of GO and RGO reduced by FeI$_2$ under different pH. The fitting of C 1s XPS spectrum of GO in Fig. 1b clearly indicates a considerable degree of oxidation with four components that correspond to carbon atoms in different functional groups: the peak at 284.8 eV is ascribed to the non-oxygenated C-C/C=C, while the peaks at 285.7, 287.2 and 287.9 eV corresponding to the C-O, C=O, and the carboxylate O-C=O groups, respectively.[28] After reduced by FeI$_2$, the C1s XPS spectrum of RGO-1 exhibited certain oxygen functionalities that can be assigned for GO (Fig. 1c), but the peak intensities of these oxygen-containing components in the RGO-1 were sharply decreased, indicating highly efficient reduction of the GO by FeI$_2$. Interestingly, comparing to GO, the XPS survey spectra for RGO always showed an additional I 3d$_{5/2}$ and I 3d$_{3/2}$ peak at 619 and 631 eV respectively, suggesting that some iodine has been incorporated into RGO (Fig. 1a). Considering the iodine atoms can be absorbed on the surface of RGO during the reduction of GO, the as-prepared RGO was washed and sonicated in ethanol for at least 20 min, and then dried at 100 ºC in vacuum for 24 h before use and characterization. The physically bonded iodine can be removed after such procedures, while the remaining iodine on the surface of RGO might has a relatively strong chemical bonding with the matrix. It has been well reported that iodine can be used as p-type dopant to improve the electrical conductivity of polymers and carbon materials[29-32]: the iodine (polyiodides I$_x^-$, usually composed of I$^-$ and I$_2$) doped in carbon nanotubes or conducting polymers can efficiently promote electron transfer from carbon nanotubes or polymer to polyiodide chain and produce a large number of mobile hole carriers, leading to an increase in electrical conductivity of carbon materials and polymers. Thus, the remnant iodine content in RGO should also contribute to the electrical conductivity.
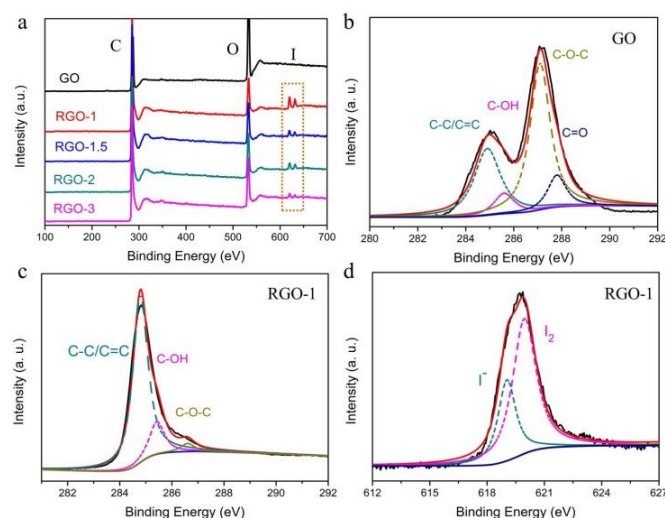

Fig. 1 (a) Full range XPS spectrum of GO and RGO reduced by FeI$_2$ under different pH; (b) High resolution XPS C1s peak of GO; High resolution XPS C1s peak (c) and XPS I 3d$_{5/2}$ peak (d) of RGO reduced by FeI$_2$ at pH=1.

The Raman spectra of GO and RGO reduced by FeI$_2$ solution under different pH is shown in Fig. 2a, recorded using 633 nm laser irradiation. The I$_D$/I$_G$ ratio of RGO increased notably after FeI$_2$ reduction compared to that of GO, indicating the restoration of the conjugated C=C bond and an increase in the number of smaller sp^2 domains after the FeI$_2$ reduction of GO to RGO.[33] The electrical conductivities at room temperature of RGO compressed-powder samples reduced by FeI$_2$ under different pH are shown in Fig. 2b. It

is much obvious that lower pH values led to higher bulk conductivities, which indicates that the presence of H^+ can efficiently improve the reductive ability by inhibiting the hydrolysis of strong Lewis acid in FeI_2 aqueous solution.[28] In addition, the RGO compressed-powder samples at pH=1 exhibited a conductivity of ~ 2600 S/m, which is almost 10 times higher than that of the compressed-powder sample of RGO reduced by hydrazine hydrate (~ 200 S/m) as reported previously.[34] Such high intrinsic conductivity of RGO power samples should be primarily ascribed to a very dense conductive network formed by cross-linking RGO sheets in RGO aggregates and quite conductive particle-to-particle interface.[34] Interestingly, the Hall effect measurements consistently showed that RGOs were of p-type nature with a carrier concentration of ~10^{19} cm^{-3} (Fig. S2†). The hole mobility at room-temperature increased from 1.72 to 7.97 as the pH value decreased from 3 to 1. The semiconductor type and mobility for GO has not been determined due to its insulting nature and the limited sensitivity of the Hall effect measurement apparatus.
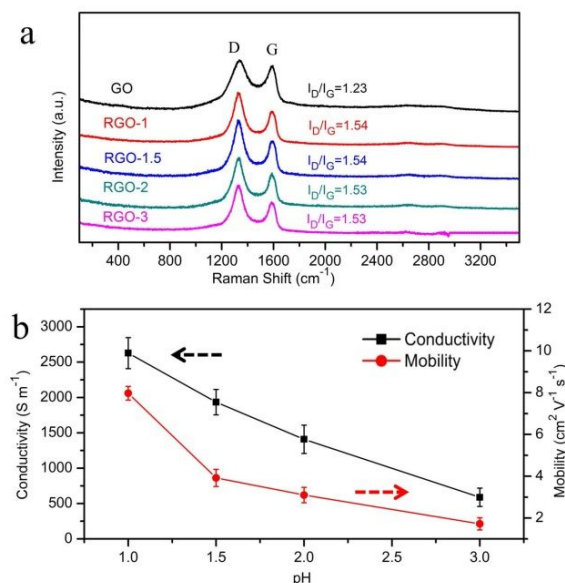

Fig. 2 (a) Raman spectra, (b) conductivities and mobilities at room temperature of RGO reduced by FeI_2 under different pH.

To evaluate the potential of applying RGO as hole extracting material for perovskite solar cells, photoluminescence (PL) was used to probe the hole quenching ability of RGO with or without dopant-free spiro-OMeTAD when interfaced with perovskite absorber. $CH_3NH_3PbI_3$ was firstly deposited on bare quartz slide and then GO or RGO with or without dopant-free spiro-OMeTAD was spin-coated on the surface of $CH_3NH_3PbI_3$ films. As shown in Fig. 3a, the PL spectrum of $CH_3NH_3PbI_3$ on bare quartz (no quencher) shows strong peak at ~ 770 nm. When RGO or GO was interfaced with perovskite, the characteristic peak intensity dramatically decreases, indicating that RGO or GO could be individually used as hole extracting material in perovskite solar cells. It is also observed that RGO quenches the perovskite steady-state PL peak more efficiently than GO. When dopant-free spiro-OMeTAD was introduced into the quenching layers, the PL quenching effect was further enhanced (Fig. 3b) due to the energetically favorable hole transfer from the perovskite to spiro-OMeTAD, which will be described later. GO with dopant-free spiro-OMeTAD shows slightly higher peak intensity than RGO/dopant-free spiro-OMeTAD composite quencher or dopant-free spiro-OMeTAD alone. However, it should be noted that the PL quenching of RGO/dopant-free spiro-OMeTAD composite quencher, shows no significant difference with respect to

that of dopant-free spiro-OMeTAD or Li-TFSI and pyridine doped spiro-OMeTAD when interfaced with perovskite. This result was probably due to that RGO could extract holes from perovskite as efficient as spiro-OMeTAD.
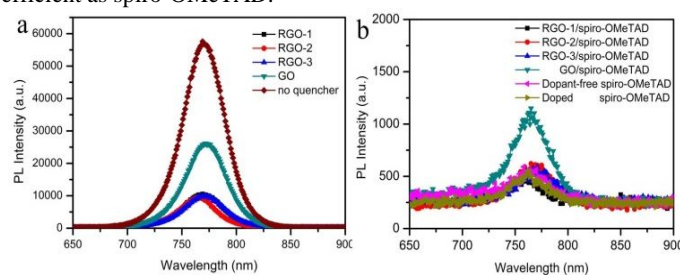

Fig. 3 Steady-state PL spectra of RGO and GO without (a), and with dopant-free spiro-OMeTAD (b) spin-coated on $CH_3NH_3PbI_3$ films.

To evaluate the presence of RGO on device performance, perovskite solar cells with $CH_3NH_3PbI_3$ as light absorber were fabricated. The $CH_3NH_3PbI_3$ perovskite layer was deposited on top of mesoporous TiO_2 scaffold using a sequential deposition method. RGO or GO was deposited on $CH_3NH_3PbI_3/TiO_2$ films by spin-coating and followed by spin-coating dopant-free spiro-OMeTAD. The solar cells were completed through depositing a layer of ~400 nm Au electrode on the RGO/spiro-OMeTAD covered film surfaces. Fig. 4a shows a typical scanning electron microscopy (SEM) top surface image of perovskite films covered by RGO. It can be clearly seen that RGO sheets lied horizontally and are anchored firmly on the perovskite surface. RGO interfaced with perovskite in horizontal directions will be beneficial to the charge extraction from perovskite. However, since RGO cannot completely cover the perovskite surface, discrete islands have been formed on perovskite surface. After spiro-OMeTAD was spin-coated, the uncovered perovskite surface was completely buried and RGO islands were partly covered as shown in Fig. 4b. The total thickness of the active layer in this work is 580 nm, consisting of 410 nm–thick perovskite filled in the mesoporous TiO_2 scaffold and 170 nm-thick perovskite capping layer. The thickness of spiro-OMeTAD is about 200 nm as shown in Figure 4c. The RGO islands were always slightly protuberant over the spiro-OMeTAD layer and finally would contact the back electrode, which could greatly benefit the charge transportation, as discussed later in the paper.
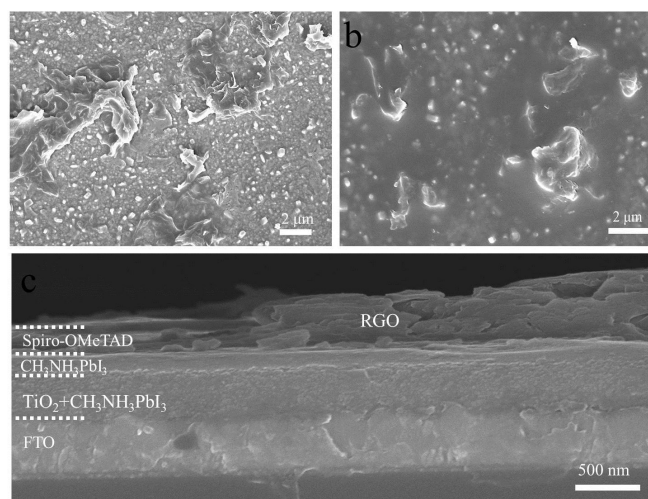

Fig. 4 Typical top view SEM images of RGO (a) and RGO/spiro-OMeTAD (b) on the surface of perovskite/TiO_2 layer; (c) typical cross-sectional SEM images of RGO/spiro-OMeTAD coated perovskite layer.
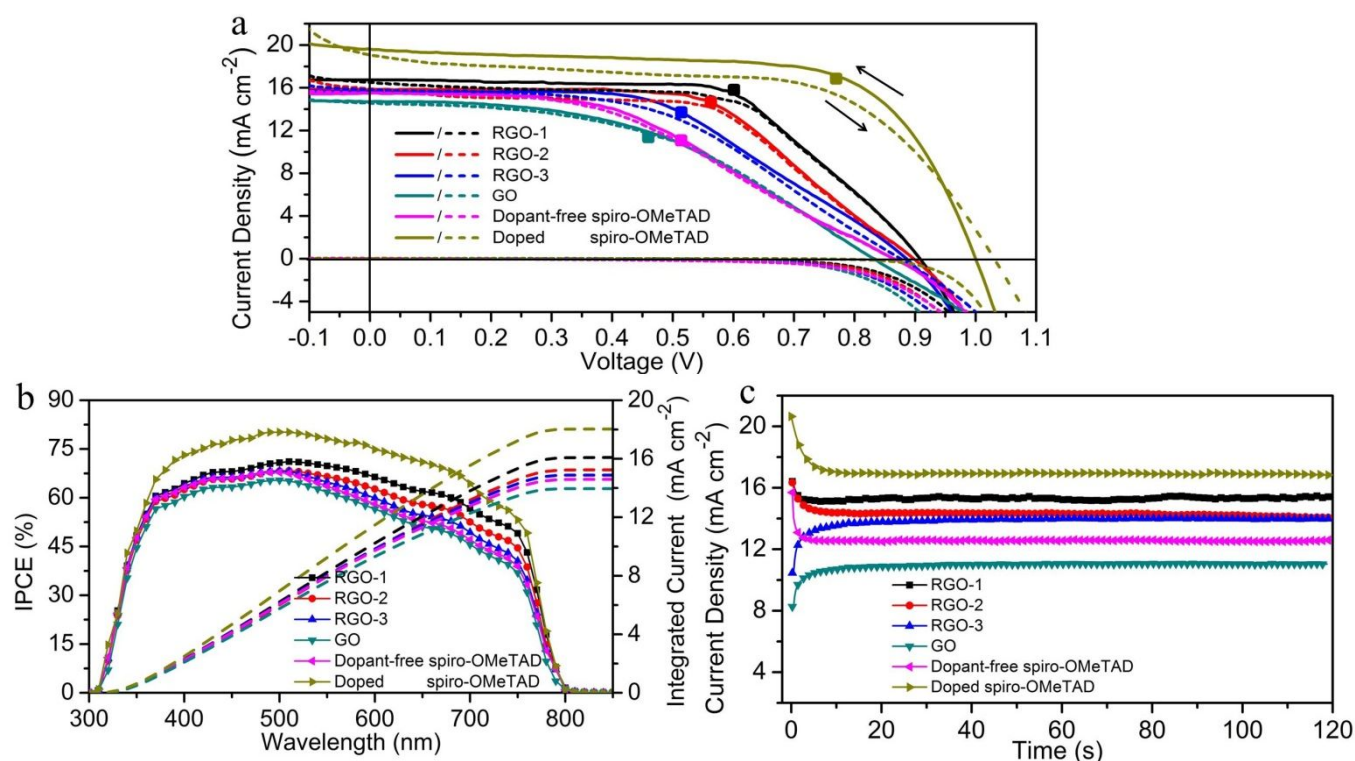
Fig. 5 (a) Forward bias to short-circuit (FB-SC, solid line) and SC-FB (dash line) *J-V* curves of perovskite solar cells with different hole transport layers. Devices were scanned at 0.022 V s^{-1}. (b) The incident photon to current efficiency spectra of perovskite solar cell with different hole transport layers and integrated current density. (c) The photocurrent density as a function of time for the cells held at a forward bias of maximum output power point (0.60, 0.56, 0.51, 0.51, 0.46 and 0.77 V for the devices based on RGO-1, RGO-2, RGO-3, GO, dopant-free spiro-OMeTAD and doped spiro-OMeTAD, respectively). The black, red, blue, magenta, dark cyan and dark yellow squarenesses on the *J-V* curves in (a) represent the value of the stabilized photocurrent density measured in (c). The cells were measured under simulated AM 1.5, 100 mW cm^{-2} solar irradiation with a cell area of 0.06 cm^2 determined by a metal mask and was placed in the dark prior to measurement.

The current density–voltage (*J-V*) characteristics for perovskite solar cells based on different hole transport layers under simulated AM 1.5, 100 mW cm^{-2} solar irradiation are shown in Fig. 5a and a summary of the device performance is tabulated in Table 1. For comparison, a reference cell fabricated with the doped spiro-OMeTAD was also prepared, which displayed a J_{sc} of 19.60, a V_{oc} of 1000 mV, and FF of 0.68, resulting in a high power conversion efficiency (PCE) of 13.33% in FB-SC scan, as shown in Figure 5a and Table 1. However, the cell with dopant-free spiro-OMeTAD exhibited, consistent with previous reports,[16] an V_{oc} of 863 mV, a J_{sc} of 15.53 mA cm^{-2}, a FF of 0.43, and a PCE of 5.85% (max. 6.5). As for the device with GO, the PCE decreased to 5.54%, even inferior to the cell with dopant-free spiro-OMeTAD, which could be due to the highly insulating nature of GO. On the other hand, when replacing GO with RGO, all the devices showed significant improvement in the photovoltaic parameters. In particular, the devices with RGO-1 and RGO-2 showed improved photovoltaic performance comparing to RGO-3-based one. RGO-1 based devices exhibited better photovoltaic performance than RGO-2-based ones. The RGO-1-based device showed an average PCE of 9.31% (max. 10.6), with a J_{sc} of 16.73, a V_{oc} of 0.910 V and a FF of 0.61. Notably, the improvements could be mainly attributed to the increased FF, which likely originate from the improved hole mobility and increased conductivity of RGO-1, as shown in Fig. 2b. However, compared to perovskite solar cells fabricated with Li-TFSI and pyridine doped spiro-OMeTAD, the *J-V* curves of the perovskite

solar cells fabricated with dopant-free spiro-OMeTAD with or without RGO have larger series resistances, which may be a result from charge extraction limited by the low conductivity of the RGO/dopant-free spiro-OMeTAD layer. The incident photo to current conversion efficiency (IPCE) spectra for the perovskite solar cells with and without RGO is shown in Fig. 5b. The photocurrent generation for different perovskite solar cells started at around 800 nm, in agreement with the observed band gap of 1.55 eV.[35] The use of RGO gave a noticeable improvement of the IPCE values in the visible to near-infrared wavelength regime, especially in the long wavelength region between 500 and 800 nm. Integrating the overlap of the IPCE spectra with the AM 1.5 G solar irradiation yield a photocurrent density of 16.08, 15.14, 14.51, 13.75, 14.31 and 18.02 mA cm^{-2} for the devices based on RGO-1, RGO-2, RGO-3, GO, dopant-free spiro-OMeTAD and doped spiro-OMeTAD, respectively, which are in general in good agreement with the measured photocurrent density. The higher IPCE values of the devices with RGO suggest that RGO were efficient to extract holes from the perovskite surface and subsequently transport them to Au back electrode. The trend of IPCE is also consistent with that of PCEs for the corresponding perovskite solar cells.

Previously, the anomalous *J-V* hysteric behavior in perovskite solar cells that has been widely observed by us and other groups,[36-39] we probed our devices to obtain their 'real' performance under working conditions. Determining the stabilized power output at a constant voltage around its maximum power point was recommended to provide reliable photovoltaic performance associated with the

Table 1 Photovoltaic parameters derived from *J-V* measurement of perovskite solar cells with and without RGO under simulated AM 1.5, 100 mW cm^{-2} solar irradiation with different scanning directions. The performance parameters were averaged over 6 devices. The stabilised PCEs were obtained from holding the bias across the cells at maximum power point derived from the FB-SC *J-V* scan until a steady state current is achieved.

Samples	Scan direction	V_{oc} [mV]	J_{sc} [mA cm^{-2}]	FF	PCE [%]	Stabilized PCE[%]
RGO-1	FB-SC	910±12	16.72±1.13	0.61±0.03	9.31±1.24	9.48
	SC-FB	906±10	16.48±1.27	0.60±0.03	8.92±0.92	
RGO-2	FB-SC	893±10	15.83±0.82	0.56±0.04	8.27±0.75	8.12
	SC-FB	891±11	15.89±0.94	0.56±0.02	7.99±0.64	
RGO-3	FB-SC	885±11	15.57±0.75	0.51±0.03	7.04±0.86	7.21
	SC-FB	881±13	15.79±0.66	0.49±0.03	6.65±0.91	
GO	FB-SC	830±13	14.53±1.10	0.46±0.04	5.54±0.68	5.63
	SC-FB	829±10	14.58±0.69	0.46±0.02	5.54±0.56	
Dopant-free spiro-OMeTAD	FB-SC	865±10	15.53±0.90	0.43±0.03	5.85±0.72	5.72
	SC-FB	863±12	15.50±0.83	0.43±0.03	5.66±0.55	
Doped spiro-OMeTAD	FB-SC	1000±12	19.60±2.25	0.68±0.02	13.33±1.64	13.01
	SC-FB	1008±12	19.02±1.83	0.61±0.04	11.85±1.35	-

devices.[38] As can be observed from Fig. 5c, for the devices with RGO-1, RGO-2, RGO-3, GO, dopant-free spiro-OMeTAD and doped spiro-OMeTAD, the photocurrent density stabilized within seconds to approximately 15.8, 14.5, 13.6, 11.0, 12.6 and 16.9 mA cm^{-2}, yielding stabilized PCEs of 9.48%, 8.12%, 7.21%, 5.63%, 5.72% and 13.01%, respectively. This indicates that our test condition provides an accurate representation for the photovoltaic performance of the devices, which is consistent with the *J-V* measurements with the FB-SC scan.
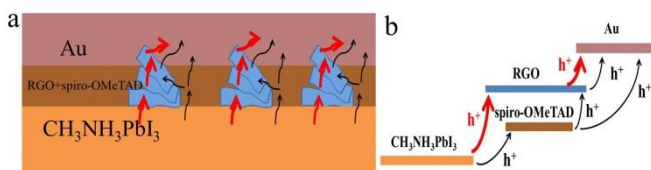

Fig. 6 (a) Schematic illustration and (b) energy levels of hole transport in completed perovskite solar cells. Blue sheet aggregates in (a) represent RGO, arrows indicate the hole transport pathways in RGO/dopant-free spiro-OMeTAD HTM.

To better explain the working mechanism when introducing RGO into the hole transport layer, a schematic illustration demonstrating the hole transport pathways is drawn for the RGO/dopant-free spiro-OMeTAD bilayer HTM (Fig. 6a). Firstly, when RGO was interfaced with perovskite, holes could be extracted from RGO/perovskite interface and subsequently transported through highly conductive RGO to metallic back electrode rapidly. Although GO also has the ability to extract holes from perovskite, the insulting nature of GO would result in rather inefficient holes transportation in GO, thus led to the photovoltaic performance decrease compared to RGO-based devices.[26,27,40] On the other hand, dopant-free spiro-OMeTAD also could extract holes from perovskite and subsequently transport them to back electrode. However, its low electrical conductivity results in relative slow hole transport rate. An alternative route for hole transport in RGO/dopant-free spiro-OMeTAD was that the holes in spiro-OMeTAD was transferred to RGO and finally reach metallic back electrode via RGO because the work function of RGO (~5.1~ ~4.90 eV)[41,42] is slightly lower than that of spiro-OMeTAD (-5.4~ 5.1 eV) (Fig. 6b).[14,43] Therefore, RGO in RGO/dopant-free spiro-OMeTAD composite plays two roles: 1) extracting holes from perovskite and transporting them to back electrode; 2) accepting holes from spiro-OMeTAD and then transporting the holes to back electrode. The two synergized routes accompanied by extraction and transportation of holes by spiro-OMeTAD led to further photovoltaic performance enhancement of RGO-based perovskite solar cells.
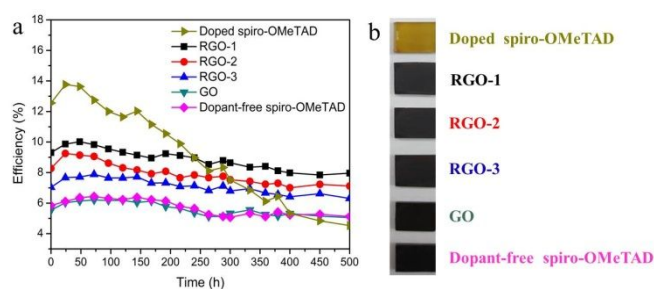

Fig. 7 (a) Efficiency stability of perovskite solar cells based on different hole transportation layers. (b) Photo images of the protective effect of different hole transport layers on the surface of perovskite/TiO$_2$ films after 500 h in air. Films and cells without encapsulation were stored in air at room temperature and cells were measured under AM 1.5, 100 mW cm^{-2} solar irradiation.

Most importantly, the commercial viability of perovskite solar cell is strongly associated with their long-term stability when subjected to real working conditions. In fact, there are many factors that influence the stability of perovskite solar cells, such as temperature, moisture and so on.[15,44] The ambient stability of perovskite solar cells fabricated with RGO and dopant-free spiro-OMeTAD as a function of storage time in dark under ambient conditions (average temperature 20±3 °C, average relative humidity 40±7%) is shown in Fig. 7 and Table 2. For comparison, the perovskite solar cell with Li-TFSI and pyridine doped spiro-OMeTAD was also tested. The perovskite solar cells based RGO or GO with dopant-free spiro-OMeTAD showed significantly improved air stability comparing with the doped spiro-OMeTAD-based device. The PCE of the RGO-1-based device remained above 85% of the initial value even after 500 h of storage in air, which is comparable with that of perovskite solar cells based on P3HT functional SWCNT encapsulated with epoxy resin and stored in nitrogen-filled glove box.[16] The rest of the RGO-based devices also demonstrated stable PCEs over 85%. In contrast, the PCE of the device fabricated with doped spiro-

OMeTAD decreased to 35% of its initial value within 500 h of storage in air, this trend is consistent with previous report in similar ambient conductions.[19] As aforementioned, the excellent stability of RGO/dopant-free spiro-OMeTAD-based devices might originate from the absence of hydrophilic Li-TSFI and the corrosive pyridine additives.

Table 2 Efficiency variations of perovskite solar cells based on RGO-1/dopant-free spiro-OMeTAD and Li-TSFI and pyridine doped spiro-OMeTAD.

Devices	PCE [%]				
	0 h	96 h	192 h	360 h	500 h
RGO-1	9.31	9.55	9.24	8.41	7.96
Doped spiro-OMeTAD	12.56	12.01	10.55	6.12	4.53

Conclusions

In conclusion, we have shown that a p-type, highly conductive RGO reduced by ferrous iodide acid aqueous solution, combined with dopant-free spiro-OMeTAD could be used as efficient HTM for stable and high efficiency perovskite solar cells. The alternative routes for holes extraction and transportation by highly conductive RGO led to photovoltaic performance enhancement of RGO-based perovskite solar cells. Device with RGO/dopant-free spiro-OMeTAD achieved a PCE of 10.6%, greatly outperforming the reference devices based on pure dopant-free spiro-OMeTAD. Furthermore, their significantly improved air stability (only 15% PCE degradation after 500 h of storage in air), compared to the device with Li-TSFI and pyridine doped spiro-OMeTAD demonstrated the potential use of hole-extraction RGO for fully replacing Li-TFSI and pyridine doping of spiro-OMeTAD. This work demonstrated that p-type and highly conductive RGO, combined with dopant-free spiro-OMeTAD, is a promising hole extraction and transportation material in stable and high-efficiency perovskite solar cells.

Acknowledgements

Notes and references

[a] State Key Laboratory of New Ceramics & Fine Processing, School of Materials Science and Engineering, Tsinghua University, Beijing 100084, P.R. China. E-mail: hong-lin@tsinghua.edu.cn

[b] College of Materials Science and Chemical Engineering, Hainan University, Haikou 570228, P. R. China.

[c] State Key Laboratory of Electronic Thin Films and Integrated Devices, University of Electronic Science and Technology of China, Chengdu 610054, P. R. China. E-mail: wangninguestc@gmail.com

† Electronic Supplementary Information (ESI) available. See DOI: 10.1039/b000000x/

‡ These authors contributed equally to this work.

1   A. Kojima, K. Teshima, Y. Shirai, T. Miyasaka, *J. Am. Chem. Soc.*, 2009, **131**, 6050.

2   J. Burschka, N. Pellet, J. Moon, S. R. Humphry-Baker, P. Gao, M. K. Nazeeruddin, M. Gratzel, *Nature*, 2013, **499**, 316.

3   M. Liu, M. B. Johnston, H. J. Snaith, *Nature*, 2013, **501**, 395.

4   M. M. Lee, J. Teuscher, T. Miyasaka, T. N. Murakami, H. J. Snaith, *Science*, 2012, **338**, 643.

5   H. Zhou, Q. Chen, G. Li, S. Luo, T. B. Song, H. S. Duan, Z. Hong, J. You, Y. Liu, Y. Yang, *Science*, 2014, **345**, 542.

6   N. J. Jeon, J. H. Noh, W. S. Yang, Y. C. Kim, S. Ryu, J. Seo, S. I. Seok, *Nature*, 2015, **517**, 476.

7   W. Nie, H. Tsai, R. Asadpour, J. C. Blancon, A. J. Neukirch, G. Gupta, J. J. Crochet, M. Chhowalla, S. Tretiak, M. A. Alam, H. Wang, A. D. Mohite, *Science*, 2015, **347**, 522.

8   J. Burschka, A. Dualeh, F. Kessler, E. Baranoff, N. L. Cevey-Ha, C. Yi, M. K. Nazeeruddin, M. Grätzel, *J. Am. Chem. Soc.*, 2011, **133**, 18042.

9   T. Leijtens, J. Lim, J. Teuscher, T. Park, H. J. Snaith, *Adv. Mater.*, 2013, **25**, 3227.

10 H. J.Snaith, M. Grätzel, *Appl. Phys. Lett.*, 2006, **89**, 262114.

11 A. Abate, T. Leijtens, S. Pathak, J. Teuscher, R. Avolio, M. E. Errico, J. Kirkpatrik, J. M. Ball, P. Docampo, I. McPherson, H. J. Snaith, *Phys. Chem. Chem. Phys.*, 2013, **15**, 2572.

12 U. B. Cappel, T. Daeneke, U. Bach, *Nano Lett.*, 2012, *12*, 4925.

13 W. Li, H. Dong, L. Wang, N. Li, X. Guo, J. Li, Y. Qiu, *J. Mater. Chem. A*, 2014, **2**, 13587.

14 W. H. Nguyen, C. D. Bailie, E. L. Unger, M. D. McGehee, *J. Phys. Chem. Lett.*, 2014, **136**, 10996.

15 S. N. Habisreutinger, T. Leijtens, G. E. Eperon, S. D. Stranks, R. J. Nicholas, H. J. Snaith, *Nano Lett.*, 2014, **14**, 5561.

16 S. N. Habisreutinger, T. Leijtens, G. E. Eperon, S. D. Stranks, R. J. Nicholas, H. J. Snaith, *J. Phys. Chem. Lett.*, 2014, **5**, 4207.

17 J. Y. Jeng, K. Chen, T. Y. Chiang, P. Lin, T. D. Tsai, Y. C. Chang, T. Guo, P. Chen, T. Wen, Y. Hsu, *Adv. Mater.*, 2014, **26**, 4107.

18 J. A. Christians, R. C. M. Fung, P. V. Kamat, *J. Am. Chem. Soc.*, 2013, **136**, 758.

19 J. Liu, Y. Wu, C. Qin, X. Yang, T. Yasuda, A. Islam, K. Zhang, W. Peng, W. Chen, L. Han, *Energy Environ. Sci.*, 2014, **7**, 2963.

20 P. Qin, S. Tanaka, S. Ito, N. Tetreault, K. Manabe, H. Nishino, M. K. Nazeeruddin, M. Grätzel, *Nat. Commun.*, 2014, **5**, 3834.

21 J. Xiao, J. Shi, H. Liu, Y. Xu, S. Lv, Y.Luo, D. Li, Q. Meng, Y. Li, *Adv. Energy Mater.*, 2015, DOI: 10.1002/aenm.201401943.

22 L. Badia, E. Mas-Marza, R. S. Sanchez, E. M. Barea, J. Bisquert, I. Mora-Sero, *APL Mat.* 2014, **2**, 081507.

23 W. H. Nyguyen, C. D. Bailie, E. L. Unger, M. D. McGehee, *J. Am. Chem. Soc.*, 2014, **136**, 10996.

24 M. Cai, V. T. Tiong, T. Hreid, J. Bell, H. Xia, *J. Mater. Chem. A*, 2015, **3**, 2784.

25 K. Yan, Z. Wei, J. Li, H. Chen, Y. Yi, X. Zheng, X. Long, Z. Wang, J. Wang, J. Xu, S. Yang, *Small*, 2015, DOI: 10.1002/smll.201403348.

26 Z. Wu, S. Bai, J. Xiang, Z. Yuan, Y. Yang, W. Cui, X. Gao, Z. Liu, Y. Jin, B. Sun, *Nanoscale*, 2014, **6**, 10505.

27 J. S. Yeo, R. Kang, S. Lee, Y. J. Jeon, N. Myoung, C. L. Lee, D. Y. Kim, J. M. Yun, Y. H. Seo, S. S. Kim, S. I. Na, *Nano Energy*, 2015, **12**, 96.

28 C. Liu, F. Hao, X. Zhao, Q. Zhao, S. Luo, H. Lin, *Sci. Rep.*, 2014, **4**, 3965.

29 N. Jung, N. Kim, S. Jockusch, N. J. Turro, P. Kim, L. Brus, *Nano Lett.*, 2009, **9**, 4133.

30 L. Grigorian, K. A. Williams, S. Fang, G. U. Sumanasekera, A. L. Loper, E. C. Dickey, S. J. Pennycook, P. C. Eklund, *Phys. Rev. Lett.*, 1998, **80**, 5560.

31 X. Zeng, T. M. Ko, *J. Polym. Sci. Pol. Phys.*, 1997, **35**, 1993.

32 R. C.Teitelbaum, S. L. Ruby, T. J. Marks, *J. Am. Chem. Soc.*, 1979, **101**, 7568.

33 H. Feng, R. Cheng, X. Zhao, X. Duan, J. Li, *Nat. Commun.*, 2013, **4**, 1539.

34 S. Stankovich, D. A. Dikin, R. D. Piner, K. A. Kohlhaas, A. Kleinhammes, Y. Jia, Y. Wu, S. T. Nguyen, R. S. Ruoff, *Carbon*, 2007, **45**, 1558.

35 F. Hao, C. C. Stoumpos, R. P. H. Chang, M. Kanatzidis, G. *J. Am. Chem. Soc.*, 2014, **136**, 8094.

36 H. S. Kim, N. G. Park, *J. Phys. Chem. Lett.*, 2014, **5**, 2927.

37 R. S. Sanchez, V. Gonzalez-Pedro, J. W. Lee, N. G. Park, Y. S. Kang, I. Mora-Sero, J. Bisquert, *J. Phys. Chem. Lett.*, 2014, **5**, 2357.

38 H. J. Snaith, A. Abate, J. M. Ball, G. E. Eperon, T.Leijtens, N. K. Noel, S. D. Stranks, J. T. W. Wang, K. Wojciechowski, W. Zhang, *J. Phys. Chem. Lett.*, 2014, **5**, 1511.

39 Y. Zhang, M. Liu, G. Eperon, T. Leijtens, D. McMeekin, M. Saliba, W. Zhang, M. D. Bastiani, A. M. Petrozza, L. Herz, M. Johnston, H. Lin, H. Snaith, *Mater. Horiz.*, 2015, **2**, 315.

40 P. Docampo, J. M. Ball, M.Darwich, G. E. Eperon, H. J. Snaith, *Nat. Comm.*, 2014, **4**, 2761.

41 H. A. Becerril, R. M. Stoltenberg, M. L. Tang, M. E. Roberts, Z. Liu, Y.Chen, D. H. Kim, B. L. Lee, S. Lee, Z. Bao, *ACS Nano*, 2010, **4**, 6343.

42 P. V.Kumar, M. Bernardi, J. C. Grossman, *ACS Nano*, 2013, **7**, 1638.

43 P. Qin, A. L. Domanski, A. K. Chandiran, R. Berger, H. J. Butt, M. I. Dar, T. Moehl, N. Tetreault, P. Gao, S. Ahmad, M. K. Nazeeruddin, M. Gratzel, *Nanoscale*, 2014, **6**, 1508.

44 G. Niu, X. Guo, L. Wang, *J. Mater. Chem. A*, 2015, **3**, 8970.

A p-type and highly conductive reduced graphene oxide combined with dopant-free spiro-OMeTAD as hole transporting layer improve the stability of perovskite solar cells.